Engineering 6 (2020) 936–943

Contents lists available at ScienceDirect

Engineering

journal homepage: www.elsevier.com/locate/eng

Research
Mechanical Engineering—Article

Mechanical Analysis and Performance Optimization for the Lunar Rover's Vane-Telescopic Walking Wheel

Lu Yang [a,b,d], Bowen Cai [a,b], Ronghui Zhang [c,d,*], Kening Li [d], Zixian Zhang [e], Jiehao Lei [f], Baichao Chen [d,g], Rongben Wang [d]

[a] Tianjin Key Laboratory for Advanced Mechatronic System Design and Intelligent Control, School of Mechanical Engineering, Tianjin University of Technology, Tianjin 300384, China
[b] National Demonstration Center for Experimental Mechanical and Electrical Engineering Education, Tianjin University of Technology, Tianjin 300384, China
[c] Guangdong Key Laboratory of Intelligent Transportation System, School of Intelligent Systems Engineering, Sun Yat-sen University, Guangzhou 510275, China
[d] College of Transportation, Jilin University, Changchun 130025, China
[e] Department of Mechanical Science and Engineering, Tokyo Institute of Technology, Tokyo 152-8550, Japan
[f] Armour College of Engineering, Illinois Institute of Technology, Chicago, IL 60616, USA
[g] China Academy of Space Technology, Beijing 100029, China

A R T I C L E I N F O

Article history:
Received 20 October 2018
Revised 28 September 2019
Accepted 29 June 2020
Available online 15 July 2020

Keywords:
Intelligent vehicle
Vane-telescopic walking wheel
Performance optimization
Vane spring
Lunar rover

A B S T R A C T

It is well-known that optimizing the wheel system of lunar rovers is essential. However, this is a difficult task due to the complex terrain of the moon and limited resources onboard lunar rovers. In this study, an experimental prototype was set up to analyze the existing mechanical design of a lunar rover and improve its performance. First, a new vane-telescopic walking wheel was proposed for the lunar rover with a positive and negative quadrangle suspension, considering the complex terrain of the moon. Next, the performance was optimized under the limitations of preserving the slope passage and minimizing power consumption. This was achieved via analysis of the wheel force during movement. Finally, the effectiveness of the proposed method was demonstrated by several simulation experiments. The newly designed wheel can protrude on demand and reduce energy consumption; it can be used as a reference for lunar rover development engineering in China.

1. Introduction

Exploring the moon has become a globally important task. One of the most important tasks in moon exploration is lunar landing, such as those achieved by Chang'e 3 (China) and Apollo 13 (USA). In the future, manned lunar landings will be carried out (China: 2025 [1–3]; USA: restart Apollo [4]). Here, the key technique lies in the trafficability characteristic of the lunar rover. That is, the newly designed lunar rover should be able to walk in the complex and harsh environment of the lunar surface. For example, the surface temperature of the moon can reach 150 °C in the daytime and drop as low as −180 °C at night, which makes the wheel technology used on earth difficult to use on the moon.

For this purpose, the wheel should have the following features: ① The lunar rover should be designed with high traction performance and carrying capacity [5–9]; and ② the rover wheel should be able to traverse obstacles [10]. There is an irregular distribution of rocks, craters, and slopes of different sizes and shapes on the surface of the moon [11–16]. The particle size and softness of lunar soil vary greatly [17].

In this regard, many kinds of wheel structure have been designed. Three have successfully landed on the moon: the elastic wheel of the former Soviet Lunokhod [18], the spring-griddle net wheel used by the American Apollo lunar roving vehicle (LRV) [4], shown in Fig. 1, and the Chinese YuTu [1,19–21], shown in Fig. 2. Other research results on wheel structure include the cylinder-conical wheel developed by Harbin Institute of Technology and the grip-hook and intelligent variable-diameter wheels designed by Beihang University, which have strong adaptability with the surface of the moon (Fig. 3) [22–24].

Of these existing designed wheels, the spring-griddle net wheel is easily deformed when the load is extremely large, the cylinder-conical wheel and the intelligent variable-diameter wheel are liable to fracture upon impact, and the grip-hook wheel has a

* Corresponding author.
E-mail address: zrh1981819@126.com (R. Zhang).

https://doi.org/10.1016/j.eng.2020.07.009
2095-8099/

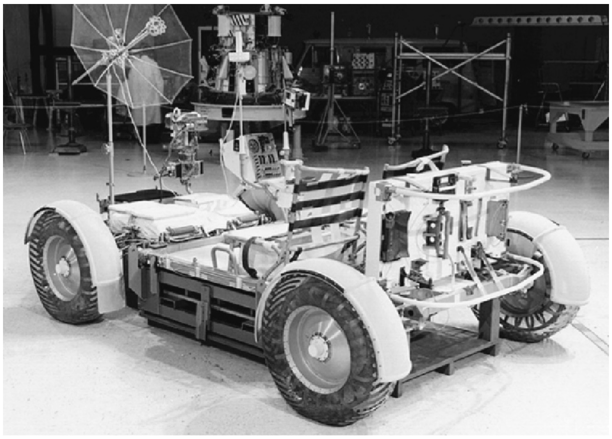

Fig. 1. The Apollo LRV.

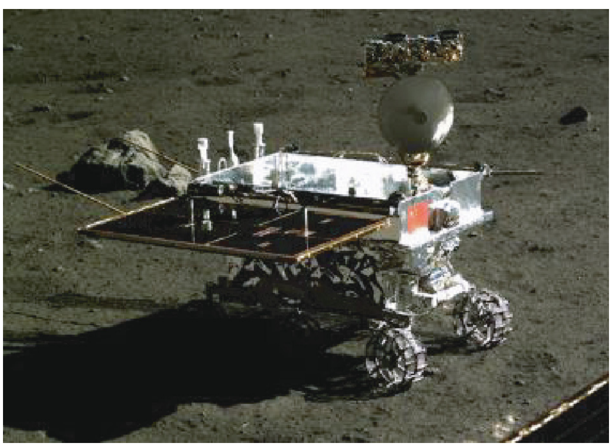

Fig. 2. YuTu and spring-griddle net wheel.

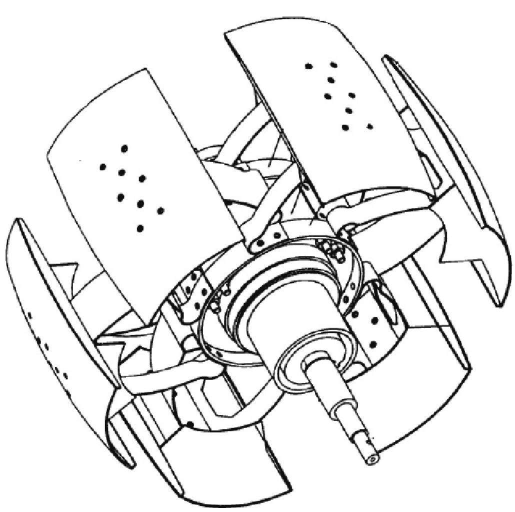

Fig. 3. The intelligent variable-diameter wheel.

complex structure and low reliability, so it is easily damaged. Furthermore, although these wheels have a strong ability to surmount obstacles, they are weak in power-consumption control and cannot meet the complex requirements of future lunar exploration projects [4]. Therefore, it is necessary to design new wheels with better balance.

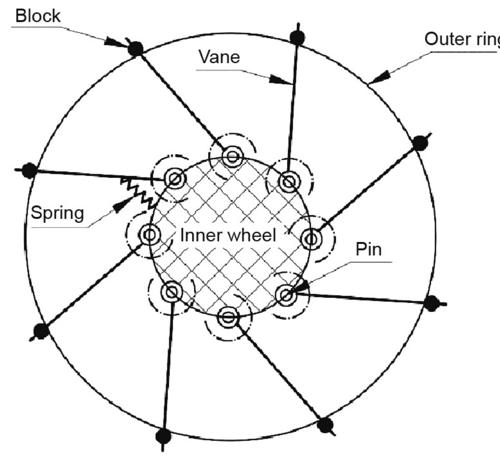

Fig. 4. Structure of vane-telescopic walking wheel.

To resolve these problems, a new wheel system is proposed. The system is based on the vane-telescopic walking wheel (Fig. 4), which was designed by the Intelligent Vehicle Group of Jilin University. This model was selected as the basis of our prototype, as it is suitable for lunar soft soil [25,26]. The most important merit of our new wheel system is that the wheel vane length can be adjusted automatically according to the road surface (i.e., softness and slope) and obstacles (i.e., size) [18].

For the vane-telescopic walking wheel, the longer the wheel vane is, the better the wheel passing performance is. Meanwhile, the greater the wheel rolling resistance is, the greater the energy consumption of the wheel is. Therefore, the ideal extension condition is for the wheel vane to protrude according to the terrain need, thus reducing the energy consumption [27].

In this study, a new wheel system is designed based on the following contributions, in order to pass through all kinds of road conditions on demand with the lowest energy consumption:

(1) A new vane-telescopic walking wheel is proposed for the lunar rover with a positive and negative quadrangle suspension.

(2) The parameters of the vane-telescopic walking wheel design are optimized.

(3) The prototype is evaluated in a simulated lunar soil environment.

(4) A new lunar rover prototype vehicle is designed and tested initially with the new wheel.

The remainder of this paper is organized as follows: Section 2 introduces the wheel force analysis for lunar rover wheels. Section 3 analyzes the parameter optimization of the vane-telescopic walking wheel design. Section 4 deals with the prototype evaluation in the simulated lunar soil environment. Section 5 concludes this paper and suggests several possible future works.

2. Force analysis for lunar rover wheels

Before optimizing the vane-telescopic walking wheel, the lunar rover wheel is analyzed based on the actual conditions on the lunar surface; the dimension of the designed wheels can then be determined based on the analysis results [28]. The paper is based on a lunar rover model with a positive and negative quadrangle suspension, which was proposed by the Intelligent Vehicle Group of Jilin University.

In Fig. 5, L_1 = 453.3 mm, L_2 = 191.65 mm, L_3 = 212.1 mm, L_4 = 218.72 mm, L_5 = 145.05 mm, L_6 = 431.86 mm, L_7 = 142.24 mm, L_8 = 342.6 mm, L_9 = 141.4 mm, L_{10} = 354.2 mm, L_{11} = 400.1 mm, L_{12} = 135 mm, γ_1 = 38.31°, γ_2 = 41.76°, γ_3 = 53.62°, γ_4 = 68.29°, γ_5 = 17.36°, γ_6 = 44.9°, γ_7 = 42.3°,

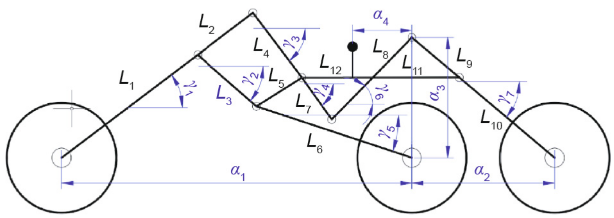

Fig. 5. Suspension rod angles and key suspension dimensions of the model.

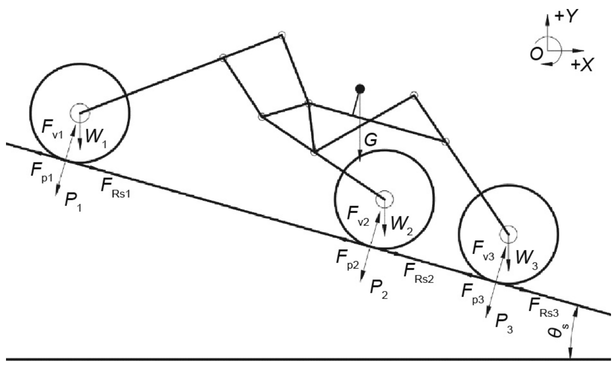

Fig. 6. The force of the mobile system on a road with a slope angel of θ_s.

Table 1
Slope resistance F_{Rs} and pressure P with varying slope θ_s.

θ_s (°)	F_{Rs1}/P_1 (N)	F_{Rs2}/P_2 (N)	F_{Rs3}/P_3 (N)
0	0/30.6	0/36.9	0/30.6
5	2.4/27.8	3.2/36.3	2.9/33.6
10	4.4/24.9	6.2/35.1	6.5/36.6
15	5.9/21.9	8.9/33.1	10.6/39.7
20	6.9/18.9	11.0/30.3	15.7/43.0
25	7.5/16.1	16.8/36.1	21.8/46.7
30	7.9/13.7	11.5/20.0	29.6/51.3

a_1 = 938.3 mm, a_2 = 359.5 mm, a_3 = 307.8 mm, and a_4 = 179.1 mm. Here, L_i is the length of suspension; whose horizontal angle is represented by γ_i; while a_i means the length between two points. According to the design requirements of the mobile system, the wheel radius R is 150 mm, the single wheel mass is 3.5 kg, and the vehicle mass is 120 kg. Under the lunar gravity field, the weight of front (W_1), middle (W_2), and rear wheels (W_3), $W_1 = W_2 = W_3$ = 5.7 N, and gravity on one side of the load platform G = 80.85 N.

The key road condition for a lunar rover is slope. In many of the road conditions that a lunar rover must pass, the slope is the most intuitive and effective factor to reflect the wheel force condition. When a lunar rover is climbing, the wheel force condition is the most serious parameter, and the traction performance requirement for the wheel is the highest priority [29]. In this paper, the wheel force analysis is carried out with a slope angel of θ_s degrees (Fig. 6).

The road's supporting force F_v and the wheel's pressure P are a pair of counterforces that have equal values and opposite directions. The friction force F_p and the slope resistance F_{Rs} are also a pair of counterforces. Therefore, the slope resistance and the pressure on the road of the lunar rover can be obtained, as shown in Table 1.

3. Optimizing parameters determination of the vane-telescopic walking wheel

The most difficult challenge is the complex lunar environment, which consists of irregular stones and craters, varying slopes, and lunar soil with varying granularity and softness. Traditional wheels cannot fully deal with such an environment because their traction ability is insufficient to pull the lunar rover in soft lunar soil. To resolve this problem, a new type of wheel is designed that can automatically retract vanes according to the soil characteristics. First, the forces between the wheels and soil are analyzed below.

3.1. Force analysis between the wheels and soil

The force of the wheel can be divided into soil thrust (ST) and soil resistance (SR) according to the effectiveness of the force. If the ST is greater than the SR, the wheel will move forward. Otherwise, the wheel will rotate or remain stationary [30–33]. Here, SR includes four kinds of resistances: soil compaction resistance (SCR), soil bulldozing resistance (SBR), soil slope resistance (SSR), and soil vane resistance (SVR) [34]. The details of ST and four kinds of SR are introduced below.

3.1.1. Compaction resistance

During the wheel rolling process, the soil is extruded vertically downward. At the same time, the soil forces the wheel to prevent the vertical extrusion from forming the wheel compaction resistance. The compaction resistance F_{Rc} can be expressed as follows [35,36]:

$$F_{Rc} = b_1 \times \left(\frac{{z_0}^{n+1}}{n+1}\right) \times \left(\frac{k_c}{b_1} + k_\varphi\right) \tag{1}$$

where z_0 is the sinking depth of the wheel rim, $z_0 = \left[\frac{3 \times P}{(k_c + b_1 \times k_\varphi) \times \sqrt{D} \times (3-n)}\right]^{\frac{2}{2n+1}}$, k_c is the cohesion modulus of the soil, k_φ is the friction modulus of the soil, n is the soil deformation index, b_1 is the width of the wheel rim, D is the diameter of the wheel rim, and P is the pressure of the wheel on the soil.

3.1.2. Bulldozing resistance

Aside from vertical compaction, soil deformation is caused by the push forward of the wheels; this is the SBR bulldozing resistance, in which the soil in front of the wheels is wave shaped [37]. The bulldozing resistance F_{Rb} can be expressed as follows:

$$F_{Rb} = b_1 \times \left(0.67 \times c \times z_0 \times K'_c + 0.5 \times {z_0}^2 \times \gamma_s \times K'_\gamma\right) \tag{2}$$

where $K'_c = [N'_c - \tan(\varphi')] \times \cos^2(\varphi')$, $K'_\gamma = [2 \times N'_\gamma/\tan(\varphi') + 1] \times \cos^2(\varphi')$, $\varphi' = \arctan[(2/3)\tan(\varphi)]$, γ_s is the bulk density, c is the cohesion force, and φ is the internal friction angle. N'_c and N'_γ are the Terzaghi bearing coefficients, which are related to φ; their values are provided in Table 2 [38–40].

3.1.3. Slope resistance

When the lunar rover climbs up a slope, the gravity in the direction of the slope creates the slope resistance [41], which can be expressed as follows:

$$F_{Rs} = W_i \times \sin(\theta_s) \tag{3}$$

where W_i is the weight of the ith wheel and θ_s is the slope angle.

Table 2
Terzaghi bearing coefficients.

φ (°)	N'_c	N'_γ
31	18	4
33	20	5
35	23	7
37	27	10
39	32	14
41	40	20

3.1.4. Vane resistance

During the rolling process, the wheel vanes compress the soil vertically, and the soil prevents the vertical extrusion force from forming the vane compacting resistance, which is known as the vane resistance [42]. The vane resistance F_{Rv} can be expressed as follows:

$$F_{Rv}=\frac{b_2\times b\times N^{n+1}\times \sin^n(180^\circ/N)\times(1-S)^{n-1}}{\pi^{n+1}\times D\times(n+1)}\times h_b^{n+1}\times\left(\frac{k_c}{b_2}+k_\varphi\right) \quad (4)$$

where N is the number of vanes, b is the vane thickness, b_2 is the vane width, S is the slip ratio of the wheel, and h_b is the inserting depth of the vane. According to the sampling analysis of the lunar soil [43], the soil deformation index n is usually equal to 1, so the slip ratio index of the wheel S is $n - 1 = 0$. Thus, the vane resistance is not affected by the wheel slip ratio.

3.1.5. Soil thrust of the vane

The maximum ST received by the wheel rim, F_w, can be expressed as follows:

$$F_w = c\times A + P\times\tan\varphi \quad (5)$$

where A is the contact area between the wheel rim and the soil: $A = 2\times b_1\times\sqrt{D\times z_0 - {z_0}^2}$.

The maximum ST received by the wheel vane, F_s, can be represented as follows:

$$F_s = b_2\times\left(\frac{1}{2}\times\gamma_s\times h_b^2\times N_\varphi + q\times h_b\times N_\varphi + 2c\times h_b\times\sqrt{N_\varphi}\right) \quad (6)$$

where q is the pressure stress of the wheel rim on the soil, $q = P/A$, N_φ is the flow value of the soil, and $N_\varphi = \tan^2(45^\circ + \varphi/2)$. According to Eqs. (1)–(6), the maximum traction force of the wheels, F_d, can be expressed by Eq. (7).

$$F_d = F_w + F_s - F_{Rc} - F_{Rb} - F_{Rs} - F_{Rv} \quad (7)$$

3.2. Optimizing parameters determination

Optimization of the vane spring, which is the most important feature for the performance of the lunar rover wheel, is our key work. In this study, the vane spring stiffness k and the spring initial torque T_0 are calculated as the optimization variables so that the wheels can endure various road conditions while consuming the lowest amount of energy.

The optimizing parameters include the minimum of the inserting depth of the vane into soil when the wheels pass h_b, the wheel rolling resistance torque T_f, the supporting force F_v, and the wheel friction force F_p. Some of the parameters are used as optimization constraints, and the others are used as the input of the optimization function. When calculating the above parameters, the following road conditions are analyzed: high, medium, and low soil passing ability; and a slope of 0°–30° [44].

By introducing the lunar soil parameters, the wheel parameters, and the wheel slope resistance F_{Rs} (Table 1), we can obtain the minimum inserting depth h_b of the vane under various passing abilities of the soil and different degrees of the slope. The wheel pressure P (Table 1) and h_b obtained above are then taken into the wheel resistance Eqs. (1), (2), and (4), and the wheel rolling resistance is obtained. The resistance is multiplied by the wheel radius R—that is, the wheel rolling resistance torque T_f. Table 3 shows the optimization parameters of the front wheel [45].

4. Optimization design and experiment with the new wheel

As shown in Fig. 7, vane 5 (i = 5) is located at the bottom of the wheel, and mainly acts with the soil. Therefore, the extension of vane 5 is considered in the following analysis. The extended length of vane 5 can be expressed as $L_{o5}(\theta_s = 0^\circ) = L_{oi}$ (i = 5, θ_s = 0°), where the calculation of function L_{o5} is detailed in the Appendix A. The objective function of the vane spring optimization is as follows:

(1) The requirement of high passing ability [46]: $L_{o5}(\theta_s)\geq h_b(\theta_s),\ \theta_s = 0^\circ,\ 5^\circ,\ \ldots,\ 30^\circ$.

(2) The requirement of reducing resistance and energy consumption [47]: $\sum[L_{o5}(\theta_s) - h_b(\theta_s)]$ must be the minimum.

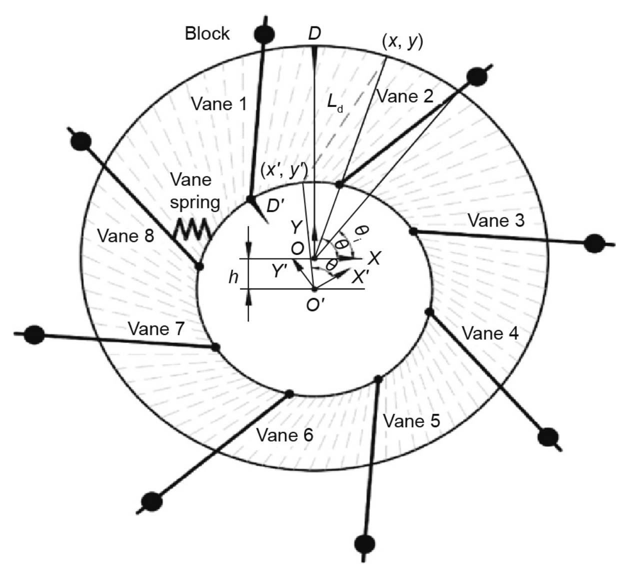

Fig. 7. The position of the vane spring.

Table 3
Optimization parameters of the front wheel.

Slope θ_s (°)	Minimum inserting depth h_b (mm)			Wheel rolling resistance torque T_f (N·mm)			Supporting force F_v (N)	Friction force F_p (N)
	High soil passing ability	Middle soil passing ability	Low soil passing ability	High soil passing ability	Middle soil passing ability	Low soil passing ability		
0	0	0	0	631.6	739.8	848.9	30.6	0
5	0	0	0	55.7	650.9	746.9	27.8	2.4
10	1.2	3.2	4.7	480.2	565.0	651.2	24.9	4.4
15	5.3	9.6	12.2	412.7	500.7	586.5	21.9	5.9
20	8.7	17.0	20.1	354.9	474.4	563.6	18.9	6.9
25	14.5	22.4	29.2	331.4	462.2	607.6	16.1	7.5
30	20.3	28.5	42.8	340.0	492.9	821.5	13.7	7.9

4.1. Optimizing the design of the vane spring

The optimization parameters obtained in Section 3.2, including T_f, F_p, F_v, and h_b, are introduced into the above objective function to obtain Eq. (8).

$$\begin{cases} L_{o5}\left(\theta_{si}\,T_{fi}\,F_{pi}\,F_{vi}\right) \geq h_{bi} \\ \sum_{i=1}^{21}\left\{L_{o5}\left(\theta_{si}\,T_{fi}\,F_{pi}\,F_{vi}\right) - h_{bi}\right\} = \text{minimum} \end{cases},\ i = 1,\ 2,\ \ldots,\ 21 \tag{8}$$

where i represents 21 kinds of road conditions, which are composed of various slopes (θ_s = 0°, 5°, 10°, 15°, 20°, 25°, and 30°) and soil passing abilities (high, medium, and low).

$$\begin{bmatrix} \theta_{s1} & T_{f1} & F_{p1} & F_{v1} \\ \theta_{s2} & T_{f2} & F_{p2} & F_{v2} \\ \vdots & \vdots & \vdots & \vdots \\ \theta_{s21} & T_{f21} & F_{p21} & F_{v21} \end{bmatrix} = \begin{bmatrix} 0 & 0.8421 & 0 & 30.6 \\ 0 & 0.9454 & 0 & 30.6 \\ 0 & 1.0489 & 0 & 30.6 \\ 5 & 0.7409 & 2.4 & 27.8 \\ 5 & 0.8439 & 2.4 & 27.8 \\ 5 & 0.9469 & 2.4 & 27.8 \\ 10 & 0.6400 & 4.4 & 24.9 \\ 10 & 0.7445 & 4.4 & 24.9 \\ 10 & 0.8499 & 4.4 & 24.9 \\ 15 & 0.5454 & 5.9 & 21.9 \\ 15 & 0.6616 & 5.9 & 21.9 \\ 15 & 0.7758 & 5.9 & 21.9 \\ 20 & 0.4600 & 6.9 & 18.9 \\ 20 & 0.6087 & 6.9 & 18.9 \\ 20 & 0.6340 & 6.9 & 18.9 \\ 25 & 0.4051 & 7.5 & 16.1 \\ 25 & 0.5700 & 7.5 & 16.1 \\ 25 & 0.6499 & 7.5 & 16.1 \\ 30 & 0.3813 & 7.9 & 13.7 \\ 30 & 0.5695 & 7.9 & 13.7 \\ 30 & 0.7893 & 7.9 & 13.7 \end{bmatrix},\quad \begin{bmatrix} h_{b1} \\ h_{b2} \\ \vdots \\ h_{b21} \end{bmatrix} = \begin{bmatrix} 0 \\ 0 \\ 0 \\ 0 \\ 0 \\ 0 \\ 0.0012 \\ 0.0032 \\ 0.0047 \\ 0.0053 \\ 0.0096 \\ 0.0122 \\ 0.0087 \\ 0.0170 \\ 0.0201 \\ 0.0145 \\ 0.0224 \\ 0.0292 \\ 0.0203 \\ 0.0285 \\ 0.0428 \end{bmatrix}$$

The spring stiffness k and initial torque value T_0 of the front wheel vanes are then obtained. According to this calculation, they are k = 0.112 N·m·rad^{-1} (1 rad = 180°/π) and T_0 = −0.038 N·m. A type of spring can be selected for the front wheel that can ensure the wheel's passing performance in the complex moon environment. It can also reduce the energy consumption from the excessive overhang of vanes [48–50].

4.2. Analysis of the optimization effect

In the function L_{o5}, the rolling resistance torque T_f and the wheel friction F_p are always formed by $T_f + R \times F_p$. $T_f + R \times F_p$ can be regarded as a variable, and is called the rolling friction force T_v. Thus, three variables in the original function L_{o5} can be expressed in the form of two variables, T_v and F_v [51]. To analyze the mechanical properties for the front wheel optimization, k = 0.112 and T_0 = 0.038 are introduced into the function $L_{o5}(k, T_0, T_f, F_p, F_v)$. The relationship between h_b, T_v, and F_v can be obtained.

Fig. 8 shows the relationship among L_{o5}, T_v, and F_v for different slopes (θ_s = 0°, 5°, 10°, 15°, 20°, 25°, and 30°). It can be seen that the vane does not extend when T_v and F_v are small. When T_v and F_v reach a certain value, the vane starts to extend, and the vane extends more with an increase of T_v and F_v [52,53]. In Fig. 8, different colors represent different slopes; they do not coincide. This situation is mainly caused by the change in the contact point between the wheel and slope [54].

Fig. 9 shows the relationship between the extension length L_{o5} and the inserting depth h_b. There are 21 values of the inserting depth h_b. It can be seen that each value does not exceed its corresponding surface, which means that $h_b \leq L_{o5}$. This indicates that

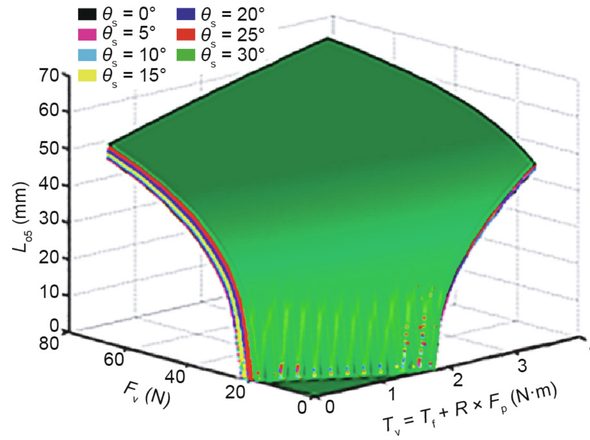

Fig. 8. Relationship among L_{o5}, T_v, and F_v for different slopes of the front wheel.

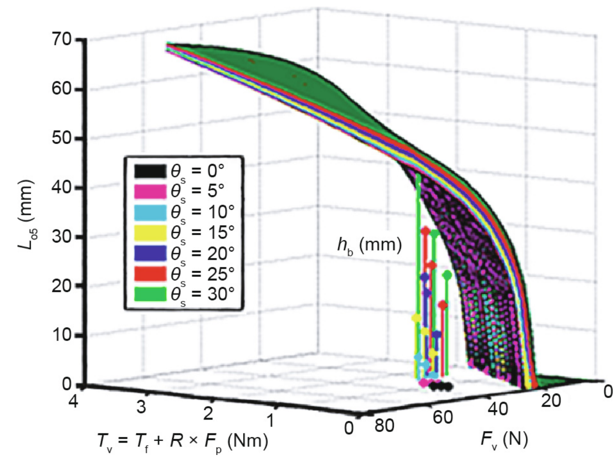

Fig. 9. Relationship between the extension length L_{o5} and the inserting depth h_b.

the vane-telescopic walking wheel can smoothly pass through the 21 kinds of road conditions [55,56]. In addition, it is clear that the maximum among the 21 values is in contact with its corresponding surface, which indicates that the wheel's energy consumption has been reduced to the lowest level.

Using the same optimization method, the spring stiffness k and initial torque value T_0 of the middle wheel are k = 0.135 N·m·rad^{-1} and T_0 = −0.023 N·m, and those of the rear wheel are k = 0.218 N·m·rad^{-1} and T_0 = −0.128 N·m.

4.3. Experiments with the vane-telescopic walking wheel

To test the actual performance and reliability of the vane-telescopic walking wheel, a prototype of the vane-telescopic walking wheel with the same dimensions was manufactured and installed on the lunar rover prototype CJ-1 (Fig. 10). An experiment on simulated lunar soil was carried out at the lunar surface simulation test field at the China Institute of Space Technology (Fig. 11).

During the test, when the lunar rover normally runs in the soil, the length of the wheel vane increases to maintain proper thrust, as shown in Fig. 12(a). Then a horizontal force of 300 N is used to pull the wheel to simulate the resistance case. The vane continues to extend and the wheel traction is increased. The increased traction force overcomes the horizontal force so that the prototype can maintain the original speed, as shown in Fig. 12(b). When the horizontal force is gradually reduced, the vane

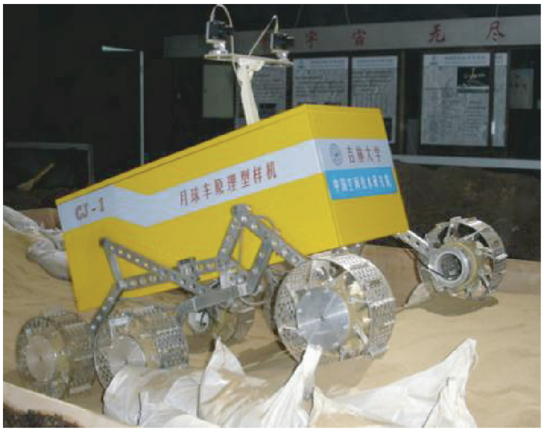

Fig. 10. Prototype of CJ-1.

is gradually restored to its original position, and the energy consumption is reduced, as shown in Fig. 12(c).

The experimental results show that the optimized vane-telescopic walking wheel can control the extension length of the vane according to the terrain resistance. Moreover, the energy consumption of the lunar rover can be effectively controlled when it passes through a complex road.

5. Conclusions

In this paper, an effective vane-telescopic walking wheel is proposed. This new walking system design method can provide a useful reference for solving the issues of trafficability and climbing ability for a lunar rover in complex terrain on the moon, while minimizing energy consumption. This was achieved through numerical simulation and system testing. First, we set up an experimental prototype, named CJ-1, to analyze the existing mechanical design. Based on the CJ-1 lunar rover prototype, a new vane-telescopic walking wheel was proposed with a positive and negative quadrangle suspension, especially designed for the complex terrain on the moon. Second, we analyzed the wheels' force for the lunar rover. Furthermore, the parameter optimization of the vane-telescopic walking wheel was analyzed and simulated. Finally, a realistic moon environment was set up to demonstrate the effectiveness of the proposed wheel system.

In future work, we aim to establish a more realistic and comprehensive test ground to simulate the lunar surface environment. More types of lunar soil can be added to allow the experiment to comprehensively simulate the real driving situation of wheels on the lunar surface. Another possible extension is to increase the bearing capacity of the vane-telescopic walking wheel for future manned lunar rovers. The Chang'e project is an important part of the National Key Project, and provides a reference for the new lunar rover design [57–61]. We would also like to have an academic exchange with researchers from all over the world.

Acknowledgements

The authors would like to show appreciation to those who have paid attention and given support to our research. We would also like to extend our thanks to the China Academy of Space Technology for providing experiment space. Besides, we would like to thanks to China–America Frontiers of Engineering (CAFOE) 2017 for providing international academic publish opportunities. We would like to have academy exchange with the researchers from all over the world about this topic. This work was supported in part by the Tianjin Natural Science Foundation of China (16JCQNJC04100) and the National Natural Science Foundation of China (61702360, 51775565, and 50675086).

Compliance with ethics guidelines

Lu Yang, Bowen Cai, Ronghui Zhang, Kening Li, Zixian Zhang, Jiehao Lei, Baichao Chen, and Rongben Wang declare that they have no conflict of interest or financial conflicts to disclose.

Fig. 11. Simulation on a lunar surface.

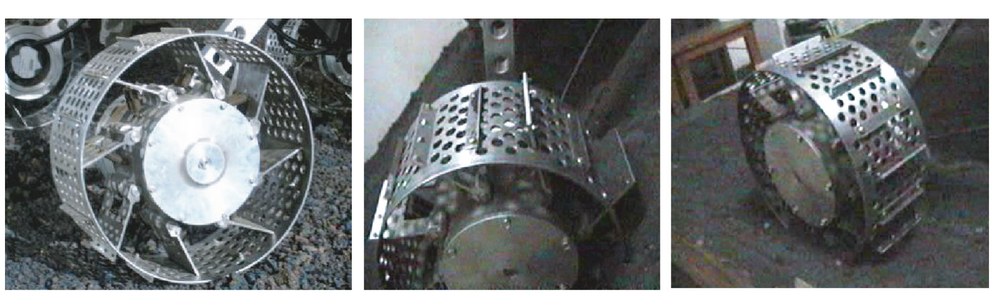

(a) (b) (c)

Fig. 12. The vane extension. (a) The length of the vane increases when running in the soil; (b) the vane continues to extend when a horizontal force is used to pull the wheel; (c) the vane is restored when the horizontal force is reduced.

Nomenclature

A	contact area between wheel rim and soil
b	vane thickness
b_1	width of the wheel rim
b_2	vane width
c	cohesion force
D	diameter of the wheel rim
F_p	wheel friction
F_v	supporting force
F_d	maximum traction force
F_{Rb}	bulldozing resistance
F_{Rc}	compaction resistance
F_{Rs}	slope resistance
F_{Rv}	vane resistance
F_w	maximum soil thrust on wheel rim
F_s	maximum soil thrust on vane
G	gravity on one side of the load platform
h	eccentricity between the inner wheel and the outer ring
h_b	inserting depth of the vane
k	vane spring stiffness
k_c	cohesion modulus of the soil
k_φ	friction modulus of the soil
L_o	length of vane extension
L_v	vane length
L_d	vane length between the outer ring and the inner wheel
N	number of vanes
n	soil deformation index
N_φ	flow value
$N_c^{'}$, $N_\gamma^{'}$	terzaghi bearing coefficient
P	wheel pressure
q	pressure stress
R	outer ring radius
r	inner wheel radius
S	slip ratio of the wheel
T_0	spring initial torque
T_f	wheel rolling resistance torque
T_v	rolling friction force
W_1, W_2, W_3	weight of front, middle, and rear wheels
z_0	sinking depth of the wheel rim
γ_s	bulk density
θ_s	slope angle
φ	internal friction angle

Appendix A. Supplementary data

Supplementary data to this article can be found online at https://doi.org/10.1016/j.eng.2020.07.009.

References

[1] Liu X, Xing Y, Mao X, Teng B, Liu Y. A method of ground-based navigation plan for Chang'e-3 Lunar Rover. In: Proceedings of the 33rd Chinese Control Conference; 2014 Jul 28–30; Nanjing, China. New York: IEEE; 2014.

[2] Wang Q, Liu J. A Chang'e-4 mission concept and vision of future Chinese lunar exploration activities. Acta Astronaut 2016;127:678–83.

[3] Li F, Ye M, Yan J, Hao W, Barriot J. The precise positioning of lunar farside lander using a four-way lander-orbiter relay tracking mode. Astrophys Space Sci 2018;363(11):1–13.

[4] Asnani V, Delap D, Creager C. The development of wheels for the Lunar Roving Vehicle. J Terramechs 2009;46(3):89–103.

[5] Zhao Y, Zhang R, Li L, Guo L, Zhang M. Walking wheel design for lunar roverand and its application simulation based on virtual lunar environment. Adv Mech Eng 2014;6:1–20.

[6] Jia Y, Dai S, Zou Y, Chen X. An overview of the scientific payloads in Chinese Chang'e-3 lunar mission. In: Proceedings of IEEE International Geoscience and Remote Sensing Symposium; 2016 Jul 10–15; Beijing, China. New York: IEEE; 2016.

[7] Wu Y, Hapke B. Spectroscopic observations of the Moon at the lunar surface. Earth Planet Sci Lett 2018;484:145–53.

[8] Hou X, Ding T, Yue H, Zhang K, Pan W, Deng Z. A simulation study on a digging-typed lunar soil sampling device and its sampling characteristics based on discrete element method. In: Proceedings of IEEE International Conference on Robotics and Biomimetics; 2015 Dec 6–9; Zhuhai, China. New York: IEEE; 2015.

[9] Chen B. Design of a new locomotion system for Lunar Rover [dissertation]. Changchun: Jilin University; 2009. Chinese.

[10] Vaughan OH. Lunar environment: design criteria models for use in lunar surface mobility studies. NASA Tech Rep 1967;13(1):665–76.

[11] Di K, Xu B, Peng M, Yue Z, Liu Z, Wan W, et al. Rock size-frequency distribution analysis at the Chang'e-3 landing site. Planet Space Sci 2016;120:103–12.

[12] Bi C, Yuan Y, Zhang R, Xiang Y, Wang Y, Zhang J. A dynamic mode decomposition based edge detection method for art images. IEEE Photonics J 2017;9(6):1–13.

[13] Bi C, Yuan Y, Zhang J, Shi Y, Wang Y, Zhang R. Dynamic mode decomposition based video shot detection. IEEE Access 2018;6:21397–407.

[14] Bi C, Fu B, Chen J, Zhao Y, Yang L, Duan Y, et al. Machine learning based fast multi-layer liquefaction disaster assessment. World Wide Web 2019;22(5):1935–50.

[15] Yang L, Wang B, Zhang R, Zhou H, Wang R. Analysis on location accuracy for the Binocular Stereo Vision system. IEEE Photonics J 2018;10(1):1–16.

[16] Yang L, Cai B, Zhang R, Li K, Wang R. Design and analysis of a new type of lunar rover suspension structure and its neural network control system. J Intell Fuzzy Syst 2018;35(1):269–81.

[17] Yu X, Fang L, Liua JF. Interaction mechanical analysis between the lunar rover wheel-leg foot and lunar soil. Procedia Eng 2012;29:58–63.

[18] Sutoh M, Otsuki M, Wakabayashi S, Hoshino T, Hashimoto T. The right path: comprehensive path planning for lunar exploration rovers. IEEE Robot Autom Mag 2015;22(1):22–33.

[19] Gao H. Development of suspension frame of new eight-wheel lunar rover. Chin J Mech Eng 2008;44(7):85.

[20] Xie X, Gao F, Huang C, Zeng W. Design and development of a new transformable wheel used in amphibious all-terrain vehicles (A-ATV). J Terramechs 2017;69:45–61.

[21] Gao Y, Spiteri C, Li CL, Zheng YC. Lunar soil strength estimation based on Chang'e-3 images. Adv Space Res 2016;58(9):1893–9.

[22] Deng Z, Fang H, Dong Y, Tao J. Research on wheel-walking motion control of Lunar Rover with six cylinder-conical wheels. In: Proceedings of International Conference on Mechatronics and Automation; 2007 Aug 5–8; Harbin, China. New York: IEEE; 2007.

[23] Chen J, Wang H. Simulation of dynamic performance influencing factors of vehicle wheel bridge load simulation system. In: Proceedings of International Conference on Mechanic Automation and Control Engineering; 2010 Jun 26–28; Wuhan, China. New York: IEEE; 2010.

[24] Sun G, Gao F, Sun P, Xu G. Mobility performance analysis of an innovation lunar rover with diameter-variable wheel. In: Proceedings of 2nd International Conference on Space Information Technology; 2007 Nov 10–11; Wuhan, China. Bellingham: SPIE; 2007.

[25] Chen B. Innovative locomotion system with high trafficability and cab smoothness for lunar rover. Chin J Mech Eng 2008;44(12):143.

[26] Chen B, Wang R, Jia Y, Guo L, Yang L. Design of a high-performance suspension for lunar rover based on evolution. Acta Astronaut 2009;64(9–10):925–34.

[27] Chen B, Wang R, Jin L, Guo L, Chen Z. Study on a vane-telescopic walking wheel for lunar rover. In: Proceedings of International Society for Terrain-Vehicle Systems; 2007 Jun 23–26; Fairbanks, AK, USA; 2007.

[28] Iizuka K, Yoshida T, Kubota T. Effect of tractive given by grousers mounted on wheels for lunar rovers on loose soil. In: Proceedings of 37th Annual Conference of the IEEE Industrial Electronics Society; 2011 Nov 7–10; Melbourne, VIC, Australia. New York: IEEE; 2011.

[29] Wettergreen D, Bapna D, Maimone M, Thomas G. Developing nomad for robotic exploration of the atacama desert. Robot Auton Syst 1999;26(2–3):127–48.

[30] Wang Y, Fan T, Yu X. Stress distribution model between lunar rover wheel-leg foot and lunar soil. Key Eng Mater 2011;474–6:797–802.

[31] Jin D, Li J, Fan S, Li H, Wang Y. Analysis on the movement effect of lunar rover wheel. Appl Mech Mater 2013;307:211–4.

[32] Jiang M, Wang X, Zheng M, Dai Y. Interaction between lugged wheel of lunar rover and lunar soil by DEM with a new contact model. In: Proceedings of the 5th NASA/ASCE Workshop on Granular Materials in Space Exploration; 2012 Apr 15–18; Pasadena, CA, USA. Reston: ASCE; 2012.

[33] Li J. Research on the interaction between lunar rover wheel and lunar soil by simulation. Trans Chin Soc Agri Mach 2008;39:1–3.

[34] Kuroda Y, Teshima T, Sato Y, Kubota T. Mobility performance evaluation of planetary rover with similarity model experiment. In: Proceedings of IEEE International Conference on Robotics and Automation; 2004 Apr 26–May 1; New Orleans, LA, USA. New York: IEEE; 2004.

[35] Chen B. Vehicle system mechanical properties. Beijing: Chinese Agricultural Machinery Publication; 1981.
[36] Meng Y, Wang Y, Xie Y, Zhou J. Wheel-terrain interaction simulation of lunar rover based on Creator/Vega. Robot 2010;32(3):369–74.
[37] Zheng Y, Ouyang Z, Wang S, Zou Y. Physical and mechanical properties of lunar regolith. J Mineral Petrol 2004;24:14–9.
[38] Nakashima H. Soil–wheel interactions. In: Encyclopedia of agrophysics encyclopedia of earth sciences series. Berlin: Springer; 2011. p. 810–3.
[39] Zou M, Li J, Zhang J, Liu G, Li Y. Traction ability of lunar rover's driving wheel on different soils. J Jilin Univ Eng Technol Ed 2010;40(1):25–9. Chinese.
[40] Wei C, Zou M, Zhao Z, Li J, Zhou G. Study on the tractive ability of lunar rover wheel by discrete element method. Appl Mech Mater 2012;215–6:964–9.
[41] Chen B, Chen D. Research on dynamic performance of wheel free wheel. Mashin/Ha-Yi Kishavarzi 1982;13(2):1–15.
[42] Zhou J, Su Y, Chi Y. Simulation of soil properties by particle flow code. Chin Geotech Eng 2006;28(3):390–6.
[43] Scott RF. The density of the lunar surface soil. J Geophys Res 1968;73(16):5469–71.
[44] Sutoh M, Nagaoka K, Nagatani K, Yoshida K. Design of wheels with grousers for planetary rovers traveling over loose soil. J Terramechs 2013;50(5–6):345–53.
[45] Jiang M, Dai Y, Cui L, Xi B. Experimental and DEM analyses on wheel–soil interaction. J Terramechs 2018;76:15–28.
[46] Cardile D, Viola N, Chiesa S, Rougier A. Applied design methodology for lunar rover elastic wheel. Acta Astronaut 2012;81(1):1–11.
[47] Xia K, Ding L, Gao H, Deng Z. Motion-control-based analytical model for wheel–soil interaction mechanics of lunar rover. In: Proceedings of the 6th International Forum on Strategic Technology; 2011 Aug 22–24; Harbin, China. New York: IEEE; 2011.
[48] Ibrahim AN, Aoshima S, Fukuoka Y. Development of wheeled rover for traversing steep slope of cohesionless sand with stuck recovery using assistive grousers. In: Proceedings of the 2016 IEEE International Conference on Robotics and Biomimetics; 2016 Dec 3–7; Qingdao, China. New York: IEEE; 2016.
[49] Nakashima H, Fujii H, Oida A, Momozu M, Kanamori H, Aoki S, et al. Discrete element method analysis of single wheel performance for a small lunar rover on sloped terrain. J Terramechs 2010;47(5):307–21.
[50] Wu S, Li L, Zhao Y, Li M. Slip ratio based traction coordinating control of wheeled lunar rover with rocker bogie. Procedia Eng 2011;15:510–5.
[51] Johnson JB, Kulchitsky AV, Duvoy P, Iagnemma K, Senatore C, Arvidson RE, et al. Discrete element method simulations of Mars Exploration Rover wheel performance. J Terramechs 2015;62:31–40.
[52] Dizqah AM, Lenzo B, Sorniotti A, Gruber P, Fallah S, De Smet J. A fast and parametric torque distribution strategy for four-wheel-drive energy-efficient electric vehicles. IEEE Trans Ind Electron 2016;63(7):4367–76.
[53] Liu S, Yan Q, Wei W. A finite element analysis of blade-wheel's strength on torqu converters based on steady operating conditions. China Mech Eng 2013;24(14):1922–6. Chinese.
[54] Iizuka K, Kubota T. Study of flexible wheels for lunar exploration rovers. J Asian Elec Vehicles 2009;7(2):1319–24.
[55] Pan W, Hou X, Tang D, Ding T, Quan Q. The study of normal force model for the flow of lunar dust particles. In: Proceedings of the 2015 International Conference on Fluid Power and Mechatronics; 2015 Aug 5–7; Harbin, China. New York: IEEE; 2015.
[56] Zhang R, He Z, Wang H, You F, Li K. Study on self-tuning tyre friction control for developing main-servo loop integrated chassis control system. IEEE Access 2017;5:6649–60.
[57] Zhou J, Li P, Zhou Y, Wang B, Zang J, Meng L. Toward new-generation intelligent manufacturing. Engineering 2018;4(1):11–20.
[58] Pan Y. Heading toward Artificial Intelligence 2.0. Engineering 2016;2(4):409–13.
[59] Chen Y. Integrated and intelligent manufacturing: perspectives and enablers. Engineering 2017;3(5):588–95.
[60] Sun XJ, Zhang H, Meng WJ, Zhang RH, Li KL, Peng T. Primary resonance analysis and vibration suppression for the harmonically excited nonlinear suspension system using a pair of symmetric viscoelastic buffers. Nonlinear Dyn 2018;94(2):1243–65.
[61] Xiong H, Zhu X, Zhang R. Energy recovery strategy numerical simulation for dual axle drive pure electric vehicle based on motor loss model and big data calculation. Complexity 2018. 4071743.